Inferring Thermal Ion Temperature and Residual Kinetic Energy from Nuclear Measurements in Inertial Confinement Fusion Implosions

K. M. WOO,[1, 2, a)] R. BETTI,[1, 2, 3] O. M. MANNION,[1, 2] C. J. FORREST,[1] J. P. KNAUER,[1] V. N. GONCHAROV,[1] P. B. RADHA,[1] D. PATEL,[1, 3] V. GOPALASWAMY,[1, 3] and V. Yu. GLEBOV[1]

[1)] *Laboratory for Laser Energetics, University of Rochester, New York 14623, USA*

[2)] *Department of Physics and Astronomy, University of Rochester, NY 14623, USA*

[3)] *Department of Mechanical Engineering, University of Rochester, NY 14623, USA*

(Dated: 5 May 2020)

In inertial confinement fusion implosion experiments, the presence of residual anisotropic fluid motion within the stagnating hot spot leads to significant variations in ion-temperature measurements using neutron time-of-flight detectors along different lines of sight. The minimum ion-temperature measurement is typically used as representative of the thermal temperature. In the presence of isotropic flows, however, even the minimum DT neutron-inferred ion temperature can be well above the plasma thermal temperature. Using both DD and DT neutron-inferred ion-temperature measurements, we show that it is possible to determine the contribution of isotropic flows and infer the DT burn-averaged thermal ion temperature. The contribution of large isotropic flows on driving the ratio of DD to DT neutron-inferred ion temperatures well below unity and approaching the lower bound of 0.8 is demonstrated in multimode simulations. The minimum DD neutron-inferred ion temperature is determined from the velocity variance analysis, accounting for the presence of isotropic flows. Being close to the DT burn-averaged thermal ion temperature, the inferred DD minimum ion temperatures demonstrate a strong correlation with the experimental yields in the OMEGA implosion database. An analytical expression is also derived to explain the effect of mode $\ell = 1$ ion-temperature measurement asymmetry on yield degradations caused by the anisotropic flows.

I. INTRODUCTION

For inertially confined imploding capsules, neutrons are produced by Deuterium-Deuterium (D-D) and Deuterium-Tritium (D-T) nuclear fusion reactions within a three-dimensionally (3-D) distorted hot spot. The neutron production rate is determined by the fusion reactivity averaged over an approximate Maxwellian distribution[1]. The width of the distribution measures the ion thermal temperature[2] or the ion thermal velocity in the center-of-mass frame of a nuclear fusion reaction. Since D and T ions are not in a complete thermal equilibrium, neutron yields produced by D-D and D-T reactions depend on slightly different ion thermal temperatures. The apparent ion temperature inferred from the width of neutron energy spectrum is averaged over all burn distributions within each fluid element with varying ion thermal temperature and density profiles in space and time. In the presence of flow effects[1,3], broadening and deviations from Maxwellian distribution occur, leading to varying apparent ion temperatures along with different lines of sight (LOS's). The temperature to describe neutron yields, however, is the ion thermal temperature or Brysk[2] ion temperature, inferred from the width of neutron energy spectrum averaged over burn distributions within each fluid element without the effects of Doppler-shift[1,3] in neutron velocities.

In National Ignition Facility implosion experiments, DD ion temperatures were inferred[4] with values well below that of DT. These experiments exhibited ratios of DD to DT ion temperatures between 0.8 and 1 and small variations in ion-temperature measurements among different lines of sight. These results indicate the presence of residual fluid motion within the hot spot at peak compression[4,5]. Consequently, apparent ion temperatures, which are inferred from the width of neutron energy spectra[2], are larger than the real thermal ion temperatures. This leads to underestimating the inferred hot-spot pressures[6] used as a performance metric for inertial confinement fusion (ICF) implosions.

For a nonstationary fusion plasma, neutron velocities are Doppler shifted[1,3,7] by fluid motions along a given LOS. The resulting width of the neutron energy spectrum is broadened. Since the fluid motion varies in space, the apparent ion temperatures, which are inferred from the width of broadened neutron energy spectra, are not only larger than the real thermal ion temperature but also vary among different LOS's. This ion temperature asymmetry is uniquely determined by the behavior of the variance of hot-spot fluid velocities[1,3]. Signatures of ion-temperature asymmetry were observed in both 3-D simulations[5,8,9] and experiments[4] dominated by low modes. The velocity variance caused by fully turbulent flows[3] is homogeneous in space. This isotropy gives rise to turbulent residual kinetic energy, which consequently inflates apparent ion temperatures uniformly in 4π.

In this work, the velocity variance analysis[9] is applied

[a)] Electronic mail: kwoo@lle.rochester.edu

to examine the 3-D effects of large isotropic flows. Strong correlations between the isotropic velocity variance and the ratio of DD to DT minimum ion temperatures are observed. (The terminology of minimum ion temperature in this work refers to the global minimum of ion temperatures measured by any detector, unless stated otherwise.) Two applications to derive the DD minimum neutron-inferred ion temperature and the DT burn-averaged thermal ion temperature are presented. The DD minimum ion temperature is derived by the removing the anisotropic velocity variance from a simultaneous DD and DT ion-temperature measurement along the same single LOS. Resulting DD minimum ion temperatures demonstrate a strong correlation with the experimental fusion yields in the OMEGA implosion database. A hot spot of an implosion subject to multi-mode velocity perturbations is shown to exhibit large isotropic flows, resulting in a neutron-inferred ion temperature that is smaller for DD neutrons than that from DT neutrons. Ti asymmetries for mode $\ell = 2$ are shown to depend on the competition between residual kinetic energies driven by the converging Rayleigh–Taylor (RT) spikes along the poles and the radially outward expanding bubble at the equator. The correlations between low-mode ion-temperature measurement asymmetries and residual kinetic energies are investigated in detail. The yield-over-clean (YOC, defined by the ratio of 3-D to 1-D fusion yields) is derived through an analytic relation depending on the ratio of maximum to minimum DT neutron-inferred ion temperatures for mode $\ell = 1$.

This paper is organized as follows: In Sec. (II), properties of the neutron energy spectra are discussed, including the Doppler velocity broadening and the treatment of flow effects. In Sec. (III), properties of the isotropic velocity variance are discussed, including the methods to derive the DD minimum ion temperature, the DT thermal ion temperatures, and the analytic relation that describes the yield degradation in terms of mode $\ell = 1$ Ti asymmetry. Section (IV) summarizes our conclusions.

II. FLOW EFFECTS IN NEUTRON DIAGNOSTICS

A. Neutron Diagnostics

In ICF experiments, hot-spot ion temperatures are inferred from the width of neutron energy spectra measured along a given LOS. The center-of-mass (CM) motion of a DT ion pair and the relative kinetic energy of DT ions in the CM frame produce the thermal velocity broadening centered at $E_0 = 14.1$ MeV, the birth energy of a neutron in a DT fusion reaction[2]:

$$\mathrm{D} + \mathrm{T} \rightarrow {}^{4}_{2}\mathrm{He}\ (3.5\ \mathrm{MeV}) + \mathrm{n}\ (14.1\ \mathrm{MeV}). \qquad (1)$$

An alpha particle gains a birth energy of 3.5 MeV from the total nuclear energy release of $Q = 17.6$ MeV. For a stationary fusion plasma, the shape of a neutron energy spectrum is a Gaussian distribution[2]. The width is given by the energy variance σ_{B}^2, which is proportional to the DT thermal ion temperature $T_{\mathrm{i}}^{\mathrm{thermal}}$:

$$\sigma_{\mathrm{B}}^2 = \frac{2m_{\mathrm{n}}T_{\mathrm{i}}^{\mathrm{thermal}}E_0}{m_{\mathrm{n}} + m_\alpha}, \qquad (2)$$

where m_{n} and m_α are neutron and alpha-particle rest masses, respectively. For a nonstationary fusion plasma, the CM frame velocity of DT ions is Doppler shifted or boosted by the fluid velocity $\vec{v}$. Non-relativistically[2], the amount of Doppler shift in the mean neutron energy μ is given by $\mu - E_0 = \vec{v}\cdot\hat{d}\sqrt{2m_{\mathrm{n}}E_0}$. The angles θ and ϕ for the LOS unit vector $\hat{d} = \sin\theta\cos\phi\hat{x} + \sin\theta\sin\phi\hat{y} + \cos\theta\hat{z}$ are measured in the laboratory frame.

Effects of Doppler shift in neutron velocities are manifested in the shape of neutron energy spectra $f_{\mathrm{LOS}}(E_{\mathrm{n}})$ observed along a given LOS. Since DT primary neutrons encounter only negligible scatterings with the cold DT shell, the shape of spectra $f_{\mathrm{LOS}}(E_{\mathrm{n}}) \approx \int \mathrm{Exp}[-(E_{\mathrm{n}} - \mu)^2/(2\sigma_{\mathrm{B}}^2)]\mathrm{d}N$ is effectively described by the superposition[9,10] of Doppler-shifted Gaussian energy spectra, produced by all fluid elements. The burn distribution $\mathrm{d}N(E_{\mathrm{n}})$ measures the number of neutrons with kinetic energy E_{n}, and $N = \int \mathrm{d}N$ is the total number of neutrons. This approach readily captures the formation of non-Gaussian spectra driven by flow effects without expensive efforts of direct numerical neutron transport modelings[11]. In experiments[12], the apparent ion temperatures $T_{\mathrm{i}}^{\mathrm{inferred}} = \triangle E_{\mathrm{FWHM}}^2(m_{\mathrm{n}} + m_\alpha)/(E_0 m_{\mathrm{n}} 16\ln 2)$ measured along a given LOS are inferred from the full width at half maximum(FWHM)[2] $\triangle E_{\mathrm{FWHM}} = \sigma_{\mathrm{B}}\sqrt{8\ln 2}$ of Gaussian-fitted neutron energy spectra from Eq. (2).

B. Flow Effects

For nonstationary fusion plasmas, the exact relation between thermal ion temperatures and flow effects is governed by the variance[1,3] of the neutron-production spectra in velocity or energy space. A brief summary of relativistic[1] neutron kinematics is given in Appendix A. By introducing the normalized burn-averaged bracket $\langle(...)\rangle = \int(...)f_{\mathrm{LOS}}(v_{\mathrm{n}}'')\mathrm{d}v_{\mathrm{n}}''/\int f_{\mathrm{LOS}}(v_{\mathrm{n}}'')\mathrm{d}v_{\mathrm{n}}''$, the statistics of neutron velocities are obtained from Eqs. (A8)–(A9). Non-relativistically, a beam of neutrons arriving at a detector, parallel to a given LOS unit vector $\hat{d}$, has the mean anisotropic neutron velocity

$$\langle v_{\mathrm{n}}''\rangle = v_0 + \langle\kappa\rangle + \langle\vec{v}\cdot\hat{d}\rangle. \qquad (3)$$

This result is obtained from the first moment of the neutron energy spectrum. Since the DT CM velocity $v_{\mathrm{cm}}^{\mathrm{DT}}$ is isotropic in space, its mean is zero, i.e., $\langle v_{\mathrm{cm}}^{\mathrm{DT}}\rangle = 0$. The shift due to DT relative kinetic energies in Eq. (A4) is small, i.e., $\langle\kappa\rangle = v_0\langle K\rangle/(2Q) \simeq 1.47\ \mathrm{km/s}\cdot\mathrm{keV}^{-1} \times 5T_{\mathrm{i,keV}}^{\mathrm{thermal}}$, where $\langle K\rangle \simeq 5T_{\mathrm{i}}^{\mathrm{thermal}}$ is used[1,2].

The general treatment of flow effects for an arbitrary shape of the neutron-production spectrum in the velocity space is given by the nth moment $m_n = \langle (w - \bar{w})^n \rangle$ with respect to a velocity variable $w \equiv v_n'' - v_0$ along the direction of $\hat{d}$. The mean is $\bar{w} \equiv \langle w \rangle = \langle \kappa \rangle + \langle \vec{v} \cdot \hat{d} \rangle$. The second moment is the velocity variance

$$\mathrm{var}[w] = \mathrm{var}\left[v_{\mathrm{cm}}^{\mathrm{DT}}\right] + \mathrm{var}\left[\kappa\right] + \mathrm{var}\left[\vec{v} \cdot \hat{d}\right] + 2\left\{\mathrm{cov}\left[v_{\mathrm{cm}}^{\mathrm{DT}}\kappa\right] + \mathrm{cov}\left[\kappa(\vec{v} \cdot \hat{d})\right] + \mathrm{cov}\left[(\vec{v} \cdot \hat{d})v_{\mathrm{cm}}^{\mathrm{DT}}\right]\right\}. \quad (4)$$

Definitions for the covariance and variance between any two scalars given by f and g are $\mathrm{cov}[fg] = \langle fg \rangle - \langle f \rangle \langle g \rangle$ and $\mathrm{var}\,[f] = \langle f^2 \rangle - \langle f \rangle^2$, respectively. Three covariances in Eq. (4) can be neglected because the CM frame velocity, the small shift κ, and the fluid velocity are independent of each other. Flow effects caused by non-Gaussian distributions are characterized by higher moments such as the skew $m_3/\mathrm{var}[w]^{3/2}$ and the kurtosis $m_4/\mathrm{var}[w]^2$.

Multiplying both sides of Eq. (4) with the DT total reactant mass $M_{\mathrm{DT}} = (m_{\mathrm{D}} + m_{\mathrm{T}})$, the neutron-inferred ion temperature $T_{\mathrm{i}}^{\mathrm{inferred}} = M_{\mathrm{DT}} \cdot \mathrm{var}\,[w]$ is shown to depend on the sum of the thermal ion temperature $T_{\mathrm{i}}^{\mathrm{thermal}} = M_{\mathrm{DT}} \cdot \mathrm{var}\left[v_{\mathrm{cm}}^{\mathrm{DT}}\right]$ and the velocity variance

$$T_{\mathrm{i}}^{\mathrm{inferred}} = T_{\mathrm{i}}^{\mathrm{thermal}} + M_{\mathrm{DT}} \cdot \mathrm{var}[\vec{v} \cdot \hat{d}]. \quad (5)$$

The magnitude of $\mathrm{var}[\kappa]$ is negligible compared with the variance of the ion thermal velocity and the variance of the hot-spot flow velocity. The effect of DT relative motion[1,13] mainly shifts the neutron velocity spectrum in the w-space by a small amount of κ along the direction of LOS, without altering the shape of the spectrum significantly. Microscopically, ion temperatures, which measure the collective random motion of ions, are represented by the variance operation. Equation (5) indicates that the variations in apparent ion temperatures are uniquely determined by the behavior of the variance of the hot-spot fluid velocities. By replacing M_{DT} with the total reactant mass M_{DD} in D–D fusion reactions, the same form is valid to describe DD inferred ion temperatures. The Brysk thermal ion temperature[2] is recovered in the limit of zero velocity variance, whereas the Murphy fully turbulent flows[3] are recovered in the limit of zero anisotropic part of $\mathrm{var}[\vec{v} \cdot \hat{d}]$.

III. ANALYSIS OF VELOCITY VARIANCE

A. Interpretation

The influence of 3-D flow effects on apparent ion temperatures is governed by the properties of velocity variance, contributed by both isotopic and anisotropic flows. For instance, isotropic flows lead to minimum apparent ion temperatures well above thermal ion temperatures. To describe this phenomenon, the method of velocity variance decomposition[9] is applied.

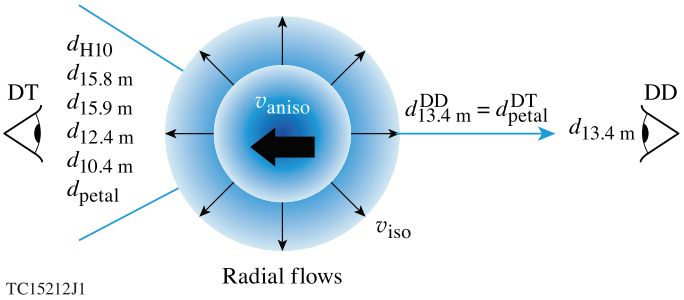

FIG. 1: A sketch for the hot-spot flow structure and the configuration[14] of seven nTOF detectors in OMEGA: six nTOF for DT's and one nTOF for DD's, to infer hot-spot ion temperatures. The petal detector for DT temperatures and the 13.4 m nTOF for DD temperatures are located at the same line of sight.

The fluid velocity vector $\vec{v} = \sum_{i=1}^{3} v_i \hat{e}_i$ and the LOS unit vector $\hat{d} = \sum_{i=1}^{3} g_i \hat{e}_i$ are substituted into the velocity variance, followed by an expansion into six components. The resulting apparent ion temperatures in Eq. (5) can be rewritten as[9]

$$T_{\mathrm{i}}^{\mathrm{inferred}} = T_{\mathrm{i}}^{\mathrm{thermal}} + M_{\mathrm{DT}} \sum_{i,j=1}^{3} g_i g_j \sigma_{ij}. \quad (6)$$

The indices correspond to Cartesian coordinates: $1 \to x$, $2 \to y$, and $3 \to z$, respectively; $\hat{e}_i$ is an orthonormal unit vector. Three geometrical factors, $g_1 = \sin\theta\cos\phi$, $g_2 = \sin\theta\sin\phi$, and $g_3 = \cos\theta$, specify the polar θ and azimuthal ϕ angles for a given LOS. The six components of velocity variance $\sigma_{ij} = \langle v_i v_j \rangle - \langle v_i \rangle \langle v_j \rangle$ measure the flow structure. For indices $i = j$, σ_{11}, σ_{22}, and σ_{33} are called "directional variance". For indices $i \neq j$, σ_{12}, σ_{23}, and σ_{31} are called "covariance". For DD temperatures, the DD total reactant mass M_{DD} is used in Eq. (6). The burn-averaged brackets for $\sigma_{ij}^{\mathrm{DD}}$ are calculated by DD burn distributions $f_{\mathrm{LOS}}^{\mathrm{DD}}$.

The interpretation for directional variance and covariance is as follows: The fluid velocity is decomposed into a burn-averaged component $\langle \vec{v}(t) \rangle$ representing the mean flow and a variation component $\triangle\vec{v}(\vec{x}, t)$ representing the perturbed flow:

$$\vec{v}(\vec{x}, t) = \langle \vec{v}(t) \rangle + \triangle\vec{v}(\vec{x}, t). \quad (7)$$

With the azimuthal symmetry, even-m single modes have zero covariances in order to conserve vanishing total translational momenta of the whole imploding capsule on the plane $P_\perp$ orthogonal to the rotation axis. Without the azimuthal symmetry, capsules for odd-m single modes translate on the plane $P_\perp$. Magnitudes of covariances for odd-m modes decrease with the azimuthal mode number because the azimuthal asymmetric flows are located within the cold bubbles, where neutron-

production rates are low. These properties reveal that covariance terms σ_{12}, σ_{23}, and σ_{31} measure the degree of azimuthal asymmetry. For 1-D spherical symmetric implosions, capsules are centered at the origin. The 1-D radial flow has zero covariances.

Since $\triangle\vec{v}$ is the perturbed component in the background of a translational mean flow $\langle\vec{v}\rangle$, the directional variance, from its defintion $\sigma_{ii} = \langle\triangle v_i \triangle v_i\rangle$, is proportional to the nontranslational component of the hot-spot fluid kinetic energy $\mathrm{KE}^{\mathrm{nontrans}}_{\mathrm{hs},i} = M_{\mathrm{hs}}\langle\triangle v_i^2\rangle/2$ along directions of three Cartesian axes $i = x, y, z$:

$$\sigma_{ii} = \langle\triangle v_i^2\rangle = 2\mathrm{KE}^{\mathrm{nontrans}}_{\mathrm{hs},i}/M_{\mathrm{hs}}, \tag{8}$$

where M_{hs} is the hot-spot mass. For turbulent flows, the terms $\triangle v_i$ can be treated as random variables with zero mean flows $\langle v_i\rangle = 0$. The covariances, which also measure the correlations among all $i \neq j$ components $\langle\triangle v_i \triangle v_j\rangle = \langle\triangle v_i\rangle\langle\triangle v_j\rangle$, asymptotically approach to zero. The flow is homogenous with respect to all LOS's. The latter are characterized by unit vectors along the radial direction originated from target chamber centers. Apparent ion temperatures $T_{\mathrm{LOS}} = T_{\mathrm{th}} + \mathrm{KE}^{\mathrm{nontrans}}_{\mathrm{hs},r} \cdot (2M_{\mathrm{DT}}/M_{\mathrm{hs}})$ are therefore inflated, uniformly in 4π, by the isotropic hot-spot fluid kinetic energies from the radial component of the flow. The velocity variance in Eq. (5) is essentially reduced to the form of isotropic velocity variance discussed in Ref.[3]

For azimuthal symmetric flows such as 2-D distorted implosions, covariances are zero. The variation in apparent ion temperatures $T_{\mathrm{LOS}} = T_{\mathrm{th}} + \sum_{i=1}^{3}\mathrm{KE}^{\mathrm{nontrans}}_{\mathrm{hs},i} g_i^2 \cdot (2M_{\mathrm{DT}}/M_{\mathrm{hs}})$ depends on the competition of nontranslational fluid kinetic energies among three orthogonal directions.

In general, as shown in Fig. (1), the 3-D hot spot contains isotropic flows originated by counterflows along the radial direction. They are not measurable in the first moment of the neutron-production spectra but broaden the width of spectra uniformly in 4π, causing $T_{\mathrm{min}} > T_{\mathrm{th}}$. The residue $\vec{v}_{\mathrm{aniso}} = \vec{v} - \vec{v}_{\mathrm{iso}}$ is the anisotropic flow, represented by an anisotropic hot-spot flow vector, as shown by the large black arrow in Fig. (1). The maximum and minimum inferred ion temperatures occur when conditions $\hat{d}_{\mathrm{LOS}} \parallel \vec{v}_{\mathrm{aniso}}$ and $\hat{d}_{\mathrm{LOS}} \perp \vec{v}_{\mathrm{aniso}}$ are satisfied, respectively.

The challenge to infer the hot-spot real thermal temperature requires separating the isotropic flows and thermal temperatures. As mentioned in Ref.[9], six DT ion-temperature measurements complete the reconstruction of the six components of the velocity variance. Whereas in this work, we show that the thermal ion temperature can be extracted by introducing a seventh measurement for the DD ion temperature along the same LOS of a DT neutron time-of-flight (nTOF) detector. The steps in Sec. (III C) – (III E) for the overall method to determine the ion thermal temperature are summarized as follows: (1) determining the anisotropic portion of the apparent DT ion temperature in the 4π angular variation from six apparent DT ion temperature observations, (2) determining the isotropic contribution from isotropic flows from by comparing the DD and DT apparent ion temperatures along a single line of site, (3) and determining the ion thermal temperature by removing the effect of the isotropic contribution from the minimum apparent DT ion temperature.

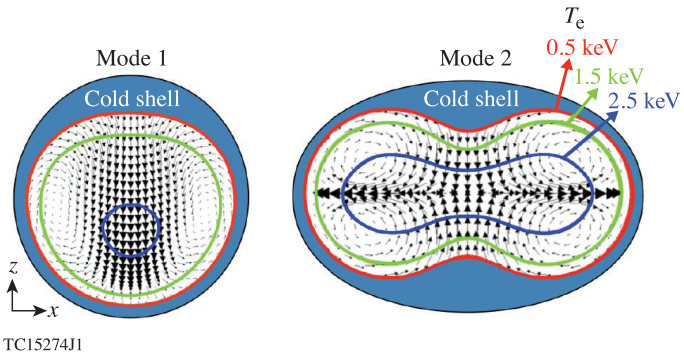

FIG. 2: Flow patterns for modes $\ell = 1$ and 2 at 7% implosion velocity perturbations. The distorted cold shell is filled with the blue color. Only flow patterns are drawn inside the hot spot bounded by the contour of $T_e = 0.5$ keV.

B. Properties of Isotropic Velocity Variance

The isotropic velocity variance is the global minimum of the velocity variance in Eq. (5). For single modes, it has a simpler form[9] given by

$$\sigma_{\mathrm{iso}}(t) = \mathrm{Min}[\sigma_{xx}(t), \sigma_{yy}(t), \sigma_{zz}(t)]. \tag{9}$$

This result is obtained by decomposing the directional variance into a constant part σ_{iso} and a varying part $\triangle\sigma_{ii} \equiv \sigma_{ii} - \sigma_{\mathrm{iso}}$ with respect to all LOS's. As discussed in Sec. (III A), covariances for single modes approach zero. Apparent ion temperatures in Eq. (6) become $T_{\mathrm{LOS}} = T_{\mathrm{th}} + M_{\mathrm{DT}}(\sigma_{\mathrm{iso}} + \sum_{i=1}^{3}\triangle\sigma_{ii} g_i^2)$, where the unit vector property $\sum_{i=1}^{3} g_i^2 = 1$ is used. Because of azimuthal symmetry, the form of isotropic velocity variance for 2-D modes is $\sigma_{\mathrm{iso}}(t) = \mathrm{Min}[\sigma_{xx}(t), \sigma_{zz}(t)]$.

The time evolution of directional variances in Eq. (9) affects the temperature measurements. A particular case is the mode $\ell = 2$ perturbation, which exhibits time-varying z-directional variances. In the rest of this work, the 3-D hydro code *DEC3D*[15] was applied to simulate the flow effects on ion-temperature measurement asymmetries caused by deceleration-phase Rayleigh-Taylor hydrodynamic instabilities. Initial radial velocity perturbations are seeded at the inner shell surface at the time of peak implosion velocity in 1-D *LILAC*[16] simulations. Effects of single modes are presented in Sec. (III B) and (III F), whereas effects of multimode are presented in Sec. (III C) and (III E). Different DD or DT ion ther-

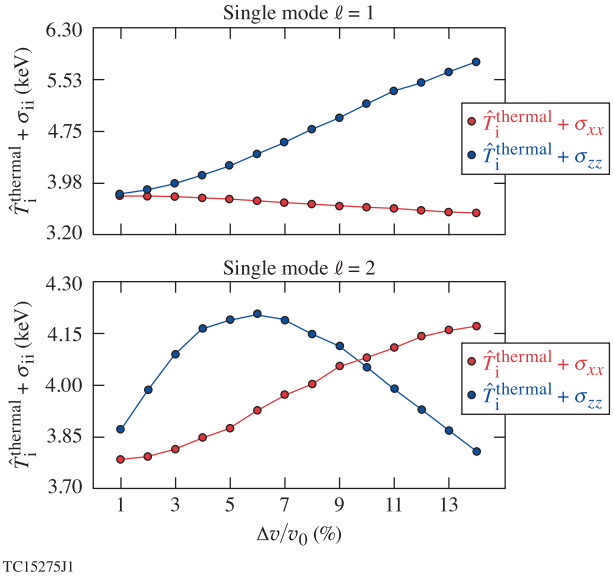

FIG. 3: Comparison of time-integrated burn-averaged directional variance $\langle\sigma_{xx}\rangle$ and $\langle\sigma_{zz}\rangle$ between modes $\ell = 1$ and 2 against different initial velocity perturbations.

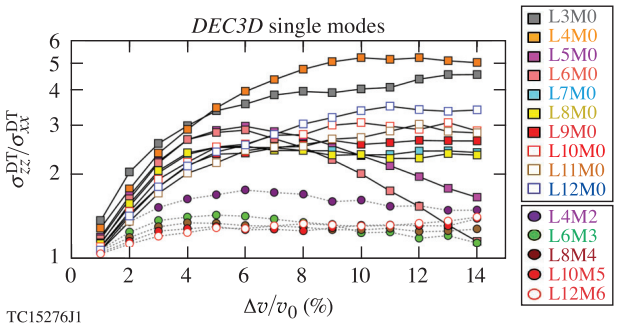

FIG. 4: The ratio of $\langle\sigma_{zz}\rangle/\langle\sigma_{xx}\rangle$ for single modes $\ell = 3$ to 12 characterizes the magnitudes of isotropic velocity variance.

mal temperatures and velocity variances are calculated by the time-integrated burn-averaged measurements in *DEC3D* simulations. As shown in Fig. (2), before the pair of RT spikes reach the center, perturbations along the poles dominate over perturbations on the equatorial plane. The latter are driven by the expanding bubble. After the RT spikes reach the center, the burn volume of the hot core along the poles is reduced significantly, leading to decreasing burn-averaged z-directional variances. Perturbations of radial flows on the equatorial plane continue to grow regardless of the initial perturbation amplitudes. As a result, the isotropic velocity variance $\sigma_{\rm iso}^{\ell=2}(t) = {\rm Min}\left[\sigma_{xx}^{\rm bubble}(t), \sigma_{zz}^{\rm spike}(t)\right]$ is governed by the competition between $\sigma_{xx}^{\rm bubble}(t)$ and $\sigma_{zz}^{\rm spike}(t)$ over time. For modest $\ell = 2$ perturbations, the time-integrated, burn-averaged z-directional variance is larger than that in the x direction and vice versa in strongly perturbed $\ell = 2$ distorted implosions.

Figure (3) compares the time-integrated burn-averaged $\langle\sigma_{xx}\rangle$ and $\langle\sigma_{zz}\rangle$ between modes $\ell = 1$ and 2 against different initial velocity perturbations. The blue and red curves represent apparent ion temperatures measured at LOS $\hat{z}$ and $\hat{x}$, respectively. Only mode $\ell = 2$ exhibits a transition from $\langle\sigma_{zz}\rangle > \langle\sigma_{xx}\rangle$ to $\langle\sigma_{zz}\rangle < \langle\sigma_{xx}\rangle$ at increasing initial velocity perturbations. This is caused by the increasingly large donut-shaped warm bubble. At a large perturbation level of 14%, the flow of $\ell = 2$ transits to anisotropic as discussed in Ref.[8]. Mode $\ell = 1$ has a vanishing isotropic velocity variance caused by the negligible $\langle\sigma_{xx}^{\ell=1}\rangle$ or $\langle\sigma_{yy}^{\ell=1}\rangle$, whereas its large ion-temperature measurement asymmetry is caused by the growing $\langle\sigma_{zz}^{\ell=1}\rangle$. Since modest perturbations are more frequent than large perturbations in high-performance ICF implosion experiments, mode $\ell = 2$ is expected to contribute significantly to the isotropic velocity variance with only a small anisotropic contribution.

Figure (4) compares the ratio of $\langle\sigma_{zz}\rangle/\langle\sigma_{xx}\rangle$ for single modes $\ell = 3$ to 12 simulated by 1%–14% implosion velocity perturbations using *DEC3D*. The x-directional variance is shown to not overtake the z-directional variance. Two-dimensional $m = 0$ modes are shown to be more anisotropic than 3-D $m \neq 0$ modes with $\langle\sigma_{zz}\rangle/\langle\sigma_{xx}\rangle > 2$. This occurs because RT spikes along the poles grow faster than spikes on the 2-D rings. As a result, velocity fluctuations in 2-D modes are slightly more anisotropic than those in 3-D modes. The latter have velocity fluctuations that are about uniform in 4π. Three-dimensional modes are shown to lie inside the range $\mathcal{R}$: $1 \leq \langle\sigma_{zz}\rangle/\langle\sigma_{xx}\rangle \leq 2$, in which the flows are close to isotropic because $\langle\sigma_{xx}\rangle$ and $\langle\sigma_{zz}\rangle$ are about equal. Two-dimensional modes $\ell = 5$ and 6 are shown to approach the range $\mathcal{R}$ at large perturbations.

The maximum isotropic velocity variance in Eq. (9) occurs when all directional variances are equal and large $\sigma_{\rm iso}^{\rm max} = {\rm Min}[\sigma_{ii} \gg 0]$; simultaneously, the anisotropic parts vanishes $\triangle\sigma_{ii} = 0$. This results in small variations in ion-temperature measurements along different LOS's. At the transition, defined by $\langle\sigma_{zz}\rangle/\langle\sigma_{xx}\rangle = 1$, from modest to large perturbations, mode $\ell = 2$ satisfies the condition to maximize the isotropic velocity variance according to Eq. (9). Mode $\ell = 2$ is a special case due to the competition of nontranslational hot-spot fluid kinetic energies between σ_{zz} and σ_{xx}. The mechanism to produce a large isotropic velocity variance requires breaking the azimuthal symmetry to form 3-D radial flow structures within the hot core, thus increasing the overall magnitudes of directional variances.

C. Properties of DD and DT Minimum Ion Temperatures

Isotropic flows are keys to account for the difference between DD and DT minimum ion temperatures:

$$T_{\rm min}^{\rm DD} = T_{\rm DD}^{\rm thermal} + M_{\rm DD}\sigma_{\rm iso}^{\rm DD},$$
$$T_{\rm min}^{\rm DT} = T_{\rm DT}^{\rm thermal} + M_{\rm DT}\sigma_{\rm iso}^{\rm DT}, \quad (10)$$

where quantities without the label "(t)"are referred to as "time-integrated, burn-averaged". Labels of $(...)_{\rm i}^{\rm inferred}$ are omitted. The ratio of DD to DT minimum ion temperatures from Eq. (10) is

$$\frac{T_{\rm min}^{\rm DD}}{T_{\rm min}^{\rm DT}} = \left(\alpha + \frac{M_{\rm DD}\sigma_{\rm iso}^{\rm DD}}{T_{\rm DT}^{\rm thermal}}\right)\left(1 + \frac{M_{\rm DT}\sigma_{\rm iso}^{\rm DT}}{T_{\rm DT}^{\rm thermal}}\right)^{-1}, \quad (11)$$

where $\alpha = T_{\rm DD}^{\rm thermal}/T_{\rm DT}^{\rm thermal}$ is the ratio of DD to DT burn-averaged thermal ion temperatures. The fraction of residual kinetic energy $f_{\rm rke}$ is defined as the ratio of the isotropic velocity variance to the DT burn-averaged thermal ion temperature:

$$f_{\rm rke} = M_{\rm DT}\sigma_{\rm iso}^{\rm DT}/T_{\rm DT}^{\rm thermal}. \quad (12)$$

In Eq. (11), about 3% small difference between $T_{\rm DD}^{\rm thermal}$ and $T_{\rm DT}^{\rm thermal}$ in *DEC3D* multi-mode simulations is observed in Sec. (III E). This observation is in close agreement with 1-D and 2-D *HYDRA* simulations for NIF highfoot implosions reported by Gatu *et. al.*[4] and Kritcher *et. al.*[17], respectively. The profile effect has a non-negligible impact to derive the thermal ion temperature in this work. Since the ratio $T_{\rm DD}^{\rm thermal}/T_{\rm DT}^{\rm thermal}$ is shown to be about constant in Sec. (III E), we account for the profile effect by treating the ratio as the averaged value obtained from simulations, i.e. $\alpha \simeq 0.97$. For hot-spot temperatures at a few keV, the diffusion mean free path of thermal ions is much less than the hot-spot radius so DT ions are rapidly thermalized through collisions. The ion-loss effect[18] on reducing hot-spot fusion reactivities is neglected, because the escaping of faster ions tends to occur at higher temperatures $\gg 10$ keV for ignition-relevant implosions. Under these conditions, ion distributions are close to the Maxwellian. At subignition temperatures $1 \sim 5$ keV, the burn-averaged velocity variances for D–D and D–T reactions are shown to be closed in Fig. (5). The ratio of DD to DT minimum inferred ion temperatures in Eq. (11) is

$$T_{\rm min}^{\rm DD}/T_{\rm min}^{\rm DT} = \left(\alpha + f_{\rm rke}\cdot\frac{M_{\rm DD}}{M_{\rm DT}}\cdot\frac{\sigma_{\rm iso}^{\rm DD}}{\sigma_{\rm iso}^{\rm DT}}\right)(1+f_{\rm rke})^{-1}. \quad (13)$$

Substituting Eq. (8) into Eq. (12),

$$f_{\rm rke} = \left(\frac{6}{1-P_{\rm e}/P_{\rm hs}}\right)\cdot\frac{{\rm KE}_{\rm hs,i,DT}^{\rm nontrans}}{{\rm IE}_{\rm hs}}, \quad (14)$$

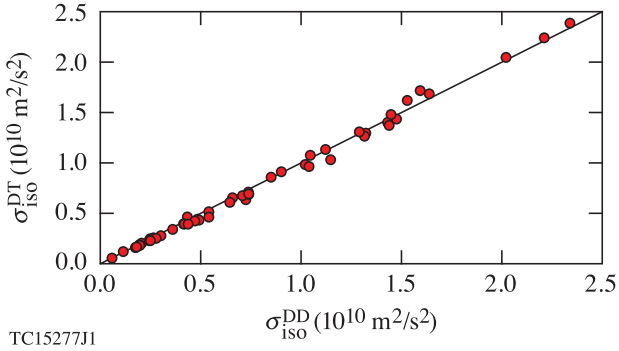

FIG. 5: Comparison of isotropic velocity variance between DD's and DT's in multimode simulations. D–D and D–T fusion reactivities are used to calculate the burn-averaged bracket for the velocity variance.

where $P_{\rm hs} = P_{\rm i} + P_{\rm e}$ is the total hot-spot pressure, $P_{\rm e/i}$ is the electron/ion pressure, ${\rm IE}_{\rm hs} = \frac{3}{2}P_{\rm hs}V_{\rm hs}$ is the total hot-spot internal energy, and $V_{\rm hs}$ is the hot-spot volume. The value within the bracket in Eq. (14) equals 12, assuming thermal equilibrium between electrons and ions, and neglects the small mass deficit in fusion reactions. In Eq. (14), $f_{\rm rke}$ measures the fraction of nontranslational isotropic hot-spot fluid kinetic energy to the hot-spot internal energy.

Murphy[3] defined the kinetic energy fraction $f_{\rm rke}^{\rm M} = E_{\rm k}^{\rm M}/(E_{\rm k}^{\rm M} + E_{\rm th}^{\rm M})$ as the ratio of the hot-spot fluid kinetic energy $E_{\rm k}^{\rm M}$ to the total hot-spot fluid energy $E_{\rm k}^{\rm M} + E_{\rm th}^{\rm M}$ such that $E_{\rm k}^{\rm M}/E_{\rm th}^{\rm M} = f_{\rm rke}/4$. Here $E_{\rm k}^{\rm M} = \frac{3}{2}M_{\rm hs}\sigma_{\rm iso}^{\rm DT}$ and $E_{\rm th}^{\rm M} = \frac{3}{2}(n_{\rm D}+n_{\rm T}+n_{\rm e})T_{\rm DT}^{\rm thermal}V_{\rm hs}$. The hot-spot mass is related to its volume by $M_{\rm hs} = \frac{1}{2}(m_{\rm D}+m_{\rm T})n_{\rm i}V_{\rm hs}$. The total hot-spot ion number density $n_{\rm i} = n_{\rm D} + n_{\rm T}$ is assumed equal to the electron number density $n_{\rm e}$ for a fully ionized DT plasma. A factor of 3 is required to express Murphy's total hot-spot kinetic energy $E_{\rm k}^{\rm M} = 3{\rm KE}_{\rm hs,i,DT}^{\rm nontrans}$ because our definition of $\sigma_{\rm iso}$ in Eq. (9) accounts for only nontranslational hot-spot fluid kinetic energy in one direction. The ratio in Eq. (13) has a lower bound of 0.8 in the limit of large $f_{\rm rke}$. At the first-order expansion with respect to small $f_{\rm rke}$ in Eq. (13),

$$T_{\rm min}^{\rm DD}/T_{\rm min}^{\rm DT} \simeq \alpha + f_{\rm rke}(0.8-\alpha), \quad (15)$$

the ratio drops linearly with the fraction of isotropic residual kinetic energy.

To approach the limit of $T_{\rm min}^{\rm DD}/T_{\rm min}^{\rm DT} \to 0.8$, more isotropic flows and lower thermal ion temperatures are required to increase $f_{\rm rke}$ in Eq. (12). Multimode perturbations satisfy this requirement because the superposition of isotropic velocity variance from modest $\ell = 2$ and 3-D $m \neq 0$ modes can lead to large isotropic flows within the hot spot. Simultaneously, large-amplitude multimode perturbations can degrade the thermal ion temperature by converting less of the shell's kinetic energies into hot-spot internal energies[15].

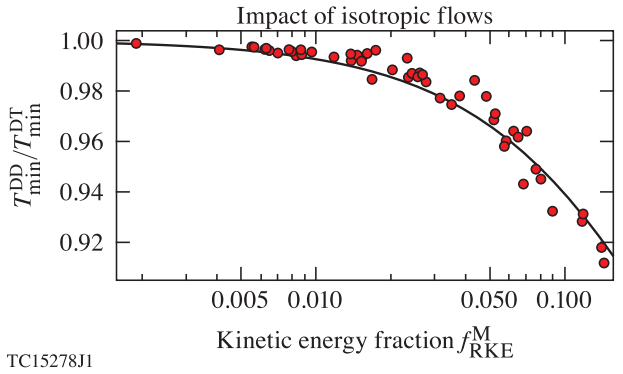

FIG. 6: Comparison of DD/DT minimum neutron-inferred ion-temperature ratio with the kinetic energy fraction $f_{\rm rke}^{\rm M}$ in multimode simulations. The black line is the analytic curve using Murphy's definition $f_{\rm rke}^{\rm M} = E_{\rm k}^{\rm M}/(E_{\rm k}^{\rm M} + E_{\rm th}^{\rm M})$ in Eq. (13).

A set of multimode simulations by superposition of the same single mode with random phases is carried out. The initial multimode velocity perturbation spectrum is given by $A_\ell^m = \sum_{i=1}^{N}(\triangle v/v_0)Y_\ell^m(\theta+\theta_i, \phi+\phi_i)$, where θ_i and ϕ_i are random phases for the ith single mode, $N = 20$ is the total number of random phases assigned for a given Y_ℓ^m single mode, and $\triangle v/v_0$ is the initial velocity perturbation.

Figure (5) shows similar isotropic velocity variance between DD's and DT's due to their small difference in temperature dependence between D–D and D–T fusion reactivities in simulations. Figure (6) shows a significant reduction of DD/DT minimum ion-temperature ratio to the level of ~ 0.9 by a rapid increase in kinetic energy fraction $f_{\rm rke}^{\rm M}$. Single-mode perturbations were observed to exhibit small values of $f_{\rm rke} < 0.3$, which is insufficient to degrade the DD/DT minimum ion-temperature ratio. The hot spot in a multimode perturbation, however, is filled with enhanced isotropic flows, and, simultaneously, the hot-spot thermal ion temperature is degraded to give a large $f_{\rm rke} \sim 0.3$ to 1 or $f_{\rm rke}^{\rm M} \sim 0.1$. A good agreement is obtained between the simulation result and the black analytic curve given by Eq. (13). The global minimum of the velocity variance var$[\vec{v}\cdot\hat{d}]$ behaves in the same way as Murphy's velocity variance in fully turbulent flows, whereas the variation part of var$[\vec{v}\cdot\hat{d}]$ contributes to ion-temperature asymmetries.

D. DD Minimum Ion Temperatures

Equation (10) indicates that the DD minimum ion temperature is closer to the thermal ion temperature than DT's, due to a smaller total fusion reactant mass $M_{\rm DD}/M_{\rm DT} = 0.8$. Consider a simultaneous ion-temperature measurement for DD and DT along the same single LOS:

$$T_{\rm DT}^{\rm LOS} = T_{\rm min}^{\rm DT} + M_{\rm DT}\sigma_{\rm aniso}^{\rm DT}, \quad (16)$$

$$T_{\rm DD}^{\rm LOS} = T_{\rm min}^{\rm DD} + M_{\rm DD}\sigma_{\rm aniso}^{\rm DD}. \quad (17)$$

As urged in Sec. (III C) , DD and DT anisotropic velocity variances are approximately the same, i.e., $\sigma_{\rm aniso}^{\rm DD} \simeq \sigma_{\rm aniso}^{\rm DT}$. The DD minimum ion temperature can be derived by removing the common anisotropic part:

$$T_{\rm min}^{\rm DD} = T_{\rm DD}^{\rm LOS} - (T_{\rm DT}^{\rm LOS} - T_{\rm min}^{\rm DT})\left(\frac{M_{\rm DD}}{M_{\rm DT}}\right). \quad (18)$$

Here the DT minimum ion temperature $T_{\rm min}^{\rm DT}$ can be either extracted from the six-LOS's method[9] by simply taking the global minimum of all available DT ion temperatures. The error propagation is about 0.3 keV for the derived $T_{\rm min}^{\rm DD}$ in Eq. (18).

Figure (7)-(a) shows a poor correlation with the DD ion temperatures measured by the 13.4 m nTOF. Figure (7)-(b) shows a strong correlation between the derived DD minimum ion temperature using Eq. (18) and the experimental yield in OMEGA implosion database. In this plot, the minimum DT ion temperatures are taken as the global minimum among all available DT temperatures. The application of the six-LOS's method is not considered here, because the current OMEGA configuration of six nTOF's for DT temperatures, as shown in Fig. (1), produces about 1-keV error. The propagated error is larger than the measurement error, which is about 0.2 keV, from the minimum measured value. To minimize the error propagation in the six-LOS's method, a new nTOF at a new line of sight has been proposed in OMEGA. The observed strong scaling $\sim T^4$ of the experimental yields with the derived DD minimum ion temperatures is in agreement with the temperature dependence for the DT fusion reactivity[19]. Since the D–D reaction has a smaller total nuclear reactant mass than DT's in Eq. (10), the derived DD minimum ion temperature is closer to the burn–averaged thermal ion temperature. This observation agrees with 2-D HYDRA simulations for NIF highfoot implosions reported by Kritcher *et. al.*[17]. In Fig. (7)-(c), the experimental yields was shown to scale as $\sim T^{3.64}$ with the measured DT minimum ion temperatures, which is slightly worse than the correlation with the derived DD minimum ion temperatures. The DT's standard deviation for the relative fitting error is shown to be slightly larger than DD's It is expected that the correlation with the thermal ion temperature is even better than either DT and DD minimum ion temperatures due to the presence of isotropic flows.

E. DT Thermal Ion Temperatures

By performing DD and DT minimum ion-temperature measurements, the degeneracy between thermal ion temperatures and isotropic flows can be recovered because

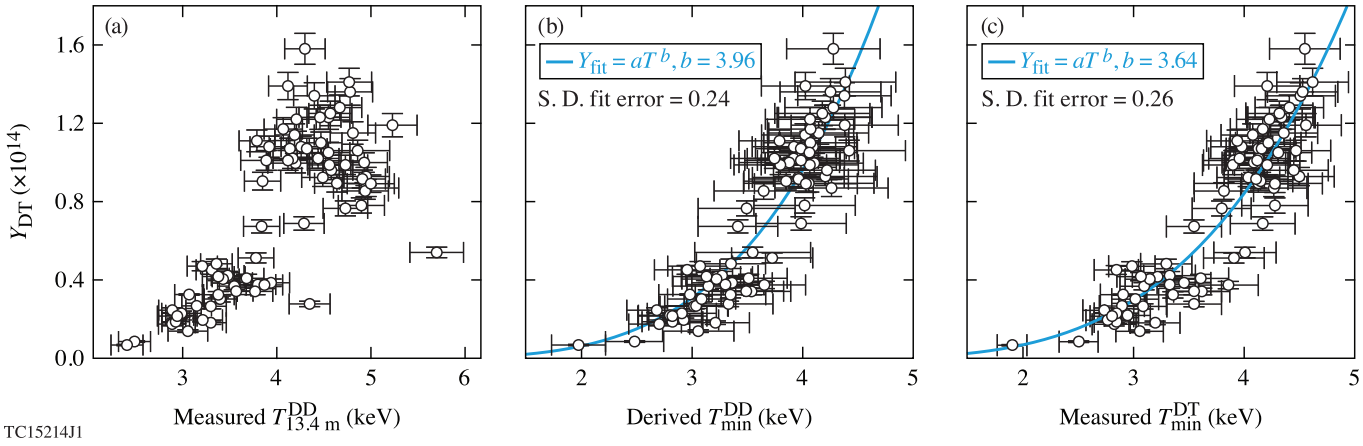

FIG. 7: Inferring for the DD minimum neutron-inferred ion temperatures in the OMEGA experiments using Eq. (18). Comparison of correlation between experimental yields and (a) the DD ion temperatures measured by the 13.4 m nTOF, (b) the derived DD minimum ion temperatures, (c) and the minimum of all measured DT ion temperatures.

TABLE I: *DEC3D* multimode perturbation (unit for temperatures is keV and $\sqrt{\sigma_{ij}}$ is km/s). The imaginary number $i = \sqrt{-1}$ is used to represent the square root of negative covariances.

Variables	$T^{thermal}_{ion}$	$T^{inferred}_{min}$	$T^{inferred}_{max}$	$\sqrt{\sigma_{11}}$	$\sqrt{\sigma_{22}}$	$\sqrt{\sigma_{33}}$	$\sqrt{\sigma_{12}}$	$\sqrt{\sigma_{23}}$	$\sqrt{\sigma_{31}}$
DD	2.86	3.47	3.83	134	152	122	34.9i	32.6i	17.4i
DT	2.95	3.72	4.20	135	154	122	36.1i	34.5i	8.86i

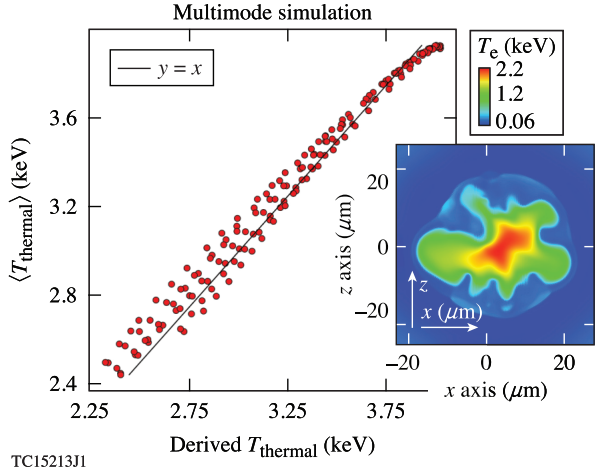

FIG. 8: Comparison of the derived and the DT burn-averaged thermal ion temperatures in *DEC3D* multimode simulation for a strongly perturbed hot spot. The inset is the 2-D x–z plane for the hot-spot temperature at stagnation.

the isotropic velocity variance is multiplied with different DD's and DT's total reactant masses. Consequently, thermal ion temperatures can be solved from Eq. (10). First, the solution of f_{rke} is expressed in terms of DD/DT minimum ion-temperature ratios using Eq. (13):

$$f_{rke} = \frac{\alpha - T^{DD}_{min}/T^{DT}_{min}}{T^{DD}_{min}/T^{DT}_{min} - R^{DD/DT}_{M} R^{DD/DT}_{\sigma}}, \qquad (19)$$

where $R^{DD/DT}_{M} \equiv M_{DD}/M_{DT}$ and $R^{DD/DT}_{\sigma} \equiv \sigma^{DD}_{iso}/\sigma^{DT}_{iso}$ are ratios of DD to DT total reactant masses and isotropic velocity variances, respectively. The DT minimum ion temperature in Eq. (10)

$$T^{DT}_{min} = T^{thermal}_{DT}\,(1 + f_{rke}) \qquad (20)$$

can be inverted to solve for the DT burn-averaged thermal ion temperature $T^{thermal}_{DT} = T^{DT}_{min}/(1+f_{rke})$ using Eq. (19). The required minimum ion temperatures can be obtained from the global minimum for DT ion temperatures reconstructed from the six-LOS's method[9] and the derived DD minimum ion temperatures in Sec. (III D). However, the derived $T^{thermal}_{DT}$ has a 4× larger error propagation than the derived T^{DD}_{min} in Eq. (18).

To solve for the thermal temperatures, the seventh temperature that should be added to the original six-LOS's ion-temperature measurements[9] is DD's. It forms an invertible LOS matrix $\hat{M}_{LOS}$ from the exact relation of Eq. (6) that describes six DT and one DD apparent ion temperatures

$$\vec{T}_7 = \hat{M}_{LOS} \cdot \vec{X}_7. \qquad (21)$$

The column vector $\vec{T}_7 = [\{T_{i=1,..,6}^{\rm DT}, T_7^{\rm DD}\}]$ contains the seven ion-temperature measurements, whereas the state vector $\vec{X}_7 = [\{\hat{T}_{\rm DT}^{\rm th}, \sigma_{11}, \sigma_{22}, \sigma_{33}, 2\sigma_{12}, 2\sigma_{23}, 2\sigma_{31}\}]M_{\rm DT}$ contains the DT thermal ion temperature and the six hot-spot flow parameters. $\hat{T}_{\rm DT}^{\rm th} = T_{\rm DT}^{\rm thermal}/M_{\rm DT}$ is the normalized DT thermal ion temperature. The explicit form for $\hat{M}_{\rm LOS}$ can be written as

$$\begin{bmatrix} 1 & g_1^1 g_1^1 & g_2^1 g_2^1 & g_3^1 g_3^1 & g_1^1 g_2^1 & g_2^1 g_3^1 & g_3^1 g_1^1 \\ 1 & g_1^2 g_1^2 & g_2^2 g_2^2 & g_3^2 g_3^2 & g_1^2 g_2^2 & g_2^2 g_3^2 & g_3^2 g_1^2 \\ 1 & g_1^3 g_1^3 & g_2^3 g_2^3 & g_3^3 g_3^3 & g_1^3 g_2^3 & g_2^3 g_3^3 & g_3^3 g_1^3 \\ 1 & g_1^4 g_1^4 & g_2^4 g_2^4 & g_3^4 g_3^4 & g_1^4 g_2^4 & g_2^4 g_3^4 & g_3^4 g_1^4 \\ 1 & g_1^5 g_1^5 & g_2^5 g_2^5 & g_3^5 g_3^5 & g_1^5 g_2^5 & g_2^5 g_3^5 & g_3^5 g_1^5 \\ 1 & g_1^6 g_1^6 & g_2^6 g_2^6 & g_3^6 g_3^6 & g_1^6 g_2^6 & g_2^6 g_3^6 & g_3^6 g_1^6 \\ \alpha & \beta g_1^7 g_1^7 & \beta g_2^7 g_2^7 & \beta g_3^7 g_3^7 & \beta g_1^7 g_2^7 & \beta g_2^7 g_3^7 & \beta g_3^7 g_1^7 \end{bmatrix}. \quad (22)$$

The matrix elements are determined by matching Eq. (6) with the state vector $\vec{X}_7$, where $\beta = M_{\rm DD}/M_{\rm DT}$. The solution for the thermal temperature and six components of velocity variance is given by $\vec{X}_7 = \hat{M}_{\rm LOS}^{-1} \cdot \vec{T}_7$. In a special case, when the seventh temperature is chosen as DT's with $\alpha = \beta = 1$ in Eq. (22), $\hat{M}_{\rm LOS}$ is not invertible. This is because in a hot spot filled with turbulent flows, all seven DT temperatures are reduced to one single apparent ion temperature $T_{\rm DT} = T_{\rm DT}^{\rm thermal} + M_{\rm DT}\sigma_{\rm iso}$ with two unknowns: thermal ion temperatures and isotropic flows. Equation (22) represents the least number of LOS's for multiple DT and DD ion-temperature measurements to separate the real thermal ion temperature from isotropic flows and the six components of velocity variance.

The existing nTOF configuration in OMEGA as shown in Fig. (1) can form the invertible LOS matrix to solve for thermal ion temperatures with about 0.8-keV errors. As a result, the correlation between experimental yields and the derived thermal ion temperatures according to the matrix inversion given by Eq. (22) is not as robust as that with the derived DD minimum ion temperatures as shown in Fig. (7) – (b). Error propagations in the matrix inversion from Eq. (22) is suppressed by adding more LOS's or reallocating the positions of LOS's.

The viability of the method to infer the thermal ion temperature is demonstrated by a *DEC3D* simulation database for strongly perturbed multimode distorted implosions as shown in Fig. (8). The spectrum of an initial multimode perturbation contains Legendre modes $\ell = 1$ to 12 including 2-D modes $m = 0$ and 3-D modes $m = \ell_{\rm even}/2$. The initial velocity perturbation is uniform for the whole spectrum. The database of multimode simulations in Fig. (8) shows that the burn-averaged $T_{\rm DD}^{\rm thermal}$ is about 3% smaller than the burn-averaged $T_{\rm DT}^{\rm thermal}$ due to the profile effect as shown in Fig. (9). This general trend can be applied to set $\alpha = 0.97$ in Eq. (22) to obtain a better agreement between the derived and the DT burn-averaged thermal ion temperatures. However, a few percent deviations from the general trend are observed. The deviations are shown to grow with perturbations, caused by the different DD and DT time-integrated neutron production profiles within a 3-D hot spot.

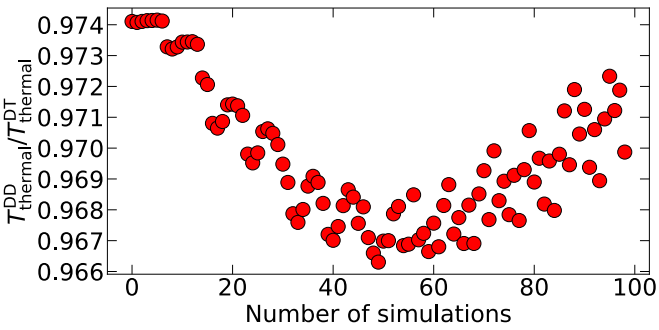

FIG. 9: Comparison of DD and DT burn-averaged thermal ion temperatures in *DEC3D* multi-mode simulations in Fig. (8).

The 2-D temperature profile for a perturbed hot spot in a sample of multimode simulations are given in Fig. (8). In this simulation, the large hot-spot flow isotropy leads to a DD/DT minimum ion-temperature ratio of $T_{\rm min}^{\rm DD}/T_{\rm min}^{\rm DT} = 0.934$ and a moderate maximum to minimum DT ion-temperature ratio of $T_{\rm max}^{\rm DT}/T_{\rm min}^{\rm DT} = 1.13$. Table (I) summarizes the thermal, the maximum and minimum inferred ion temperatures, as well as the six hot-spot flow parameters in this simulation. The square roots of three directional variances give the magnitudes of nontranslational velocity fluctuations $\sqrt{\langle \triangle v_i \triangle v_i \rangle} \sim 100$ km/s, in which the magnitude is close to the DT ions' thermal velocity given by $\sqrt{T_{\rm i,DT}^{\rm thermal}/(m_{\rm D} + m_{\rm T})} = 238$ km/s. Differences between DD and DT directional variances and covariances are observed to be small, as discussed in Sec. (III C).

F. Residual Kinetic Energy

Another application of Ti asymmetry is to describe yield degradations in the presence of large anisotropic flows. Previous studies[15,20] showed that the YOC is a strong function of the RKE:

$$\text{YOC} \simeq (1 - \text{RKE}_{\rm tot})^{\mu} \quad (23)$$

for implosions perturbed by low modes. The normalized total residual kinetic energy at stagnation is $\text{RKE}_{\rm tot} = \text{RKE}_{\rm hs} + \text{RKE}_{\rm sh}$ and $\mu = 4.4$ to 5.5. The normalized hot-spot and shell residual kinetic energies are defined as $\text{RKE}_{\rm hs} = (\text{KE}_{\rm hs}^{\rm 3D} - \text{KE}_{\rm hs}^{\rm 1D})_{\rm stag}/\text{KE}_{\rm max}^{\rm 1D}$ and $\text{RKE}_{\rm sh} = (\text{KE}_{\rm sh}^{\rm 3D} - \text{KE}_{\rm sh}^{\rm 1D})_{\rm stag}/\text{KE}_{\rm max}^{\rm 1D}$, respectively. Here $\text{KE}_{\rm hs}^{\rm 3D/1D}$ and $\text{KE}_{\rm sh}^{\rm 3D/1D}$ are the 3-D/1-D hot-spot fluid kinetic energy and the 3-D/1-D total shell kinetic energy, respectively. $\text{KE}_{\rm max}^{\rm 1D}$ is the maximum 1-D in-flight shell's kinetic energy. To apply this result in experiments, RKE must be interpreted in terms of observables of implosion asymmetries.

For mode $\ell = 1$, the ratio of maximum to minimum neutron-inferred ion temperature is dominated by the nontranslational hot-spot fluid kinetic energy along the direction of the jet. For initial velocity perturbations in the form of spherical harmonics, the jet of mode $\ell = 1$ without any phase shift in *DEC3D*[15] simulations is parallel to the z axis. For single-mode perturbations, the covariances are zero, so that the ratio of maximum $\hat{T}^{\rm DT}_{\rm max}(\theta = 0)$ to minimum $\hat{T}^{\rm DT}_{\rm min}(\theta = \pi/2)$ neutron-inferred ion temperature is

$$\left(\frac{T^{\rm DT}_{\rm max}}{T^{\rm DT}_{\rm min}}\right)_{\ell=1} = \frac{\hat{T}^{\rm thermal}_{\rm i} + \sigma^{\rm DT}_{\rm iso} + \triangle\sigma^{\rm DT}_{33}}{\hat{T}^{\rm thermal}_{\rm i} + \sigma^{\rm DT}_{\rm iso}}. \quad (24)$$

Since mode $\ell = 1$ has negligible nontranslational fluid kinetic energies $\triangle\sigma_{11} = \triangle\sigma_{22} \to 0$ along x, y directions, the isotropic velocity variance in Eq. (9) is approximately zero $\sigma^{\rm DT}_{\rm iso} \to 0$. The anisotropic velocity variance is reduced to the z-directional variance, i.e., $\triangle\sigma^{\rm DT}_{33} = \sigma^{\rm DT}_{33} - \sigma^{\rm DT}_{\rm iso} \simeq \sigma^{\rm DT}_{33}$ such that $\left(T^{\rm DT}_{\rm max}/T^{\rm DT}_{\rm min}\right)_{\ell=1} \simeq 1 + \sigma^{\rm DT}_{33}/\hat{T}^{\rm thermal}_{\rm i}$. We define the fraction of the total nontranslational hot-spot fluid kinetic energy as $f^{\rm total}_{\rm rke} = f_{\rm rke} + f^{\rm aniso}_{\rm rke}$, where the isotropic part $f_{\rm rke}$ is given by Eq. (12) and the anisotropic part is $f^{\rm aniso}_{\rm rke} = \triangle\sigma_{ii}/\hat{T}^{\rm thermal}_{\rm i}$. By substituting $f^{\rm total}_{\rm rke} = \sigma^{\rm DT}_{33}/\hat{T}^{\rm thermal}_{\rm i}$, the Ti ratio in Eq. (24) is rewritten as

$$\left(T^{\rm DT}_{\rm max}/T^{\rm DT}_{\rm min}\right)_{\ell=1} \simeq 1 + f^{\rm total}_{\rm rke}. \quad (25)$$

Two approximate hot-spot fluid properties for mode $\ell = 1$, observed from large ensembles of *DEC3D* deceleration-phase simulations, are used in the following derivations: The first property is

$$M^{\rm 3D}_{\rm hs}\sigma^{\rm DT}_{33}/2 \simeq {\rm KE}^{\rm 3D}_{\rm hs}/3, \quad (26)$$

such that the flow structure of mode $\ell = 1$ approximately satisfies $\langle\triangle v^2_3\rangle \simeq \langle v^2_3\rangle/3$. This relation is shown in Fig. (10)–(a). The expression for $f^{\rm total}_{\rm rke}$ is obtained by replacing the isotropic nontranslational hot-spot fluid kinetic energy with $M^{\rm 3D}_{\rm hs}\sigma_{33}/2$ in Eq. (14). The latter is one third of the total hot-spot residual kinetic energy by Eq. (26) so that $f^{\rm total}_{\rm rke} \simeq 4{\rm KE}^{\rm 3D}_{\rm hs}/{\rm IE}^{\rm 3D}_{\rm hs}$, where ${\rm IE}^{\rm 3D}_{\rm hs}$ is the 3-D hot-spot internal energy. The ratio of 3-D hot-spot kinetic energy to internal energy is rewritten as

$${\rm KE}^{\rm 3D}_{\rm hs}/{\rm IE}^{\rm 3D}_{\rm hs} = \left(\frac{{\rm IE}^{\rm 1D}_{\rm hs}}{{\rm IE}^{\rm 3D}_{\rm hs}}\right)\left(\frac{{\rm KE}^{\rm 1D}_{\rm max}}{{\rm IE}^{\rm 1D}_{\rm hs}}\right)\left(\frac{{\rm KE}^{\rm 3D}_{\rm hs}}{{\rm KE}^{\rm 1D}_{\rm max}}\right). \quad (27)$$

Three different terms on the right-hand side of Eq. (27) are (1) ${\rm IE}^{\rm 3D}_{\rm hs}/{\rm IE}^{\rm 1D}_{\rm hs} = 1 - {\rm RKE}_{\rm tot}$, which results from the conservation of total energy at stagnation[15]; (2) ${\rm IE}^{\rm 1D}_{\rm hs}/{\rm KE}^{\rm 1D}_{\rm max} \simeq 1/2$, which is a good approximation for 1-D implosions because typically about a half of the shell maximum kinetic energy is converted into the hot-spot internal energy at stagnations; and (3) ${\rm KE}^{\rm 3D}_{\rm hs}/{\rm KE}^{\rm 1D}_{\rm max} \simeq {\rm RKE}_{\rm tot}/2$ using the second property ${\rm RKE}_{\rm hs} \simeq {\rm RKE}_{\rm sh}$.

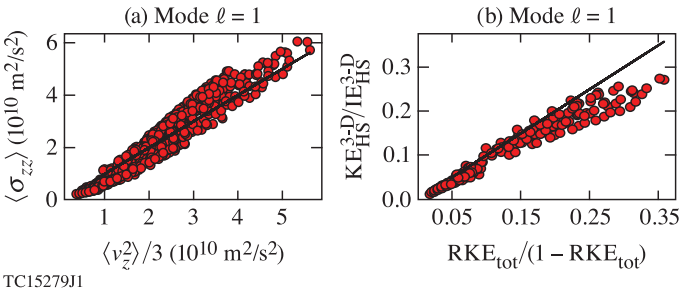

FIG. 10: Survey of fluid properties for mode $\ell = 1$: (a) for the first property of $\langle\triangle v^2_3\rangle \simeq \langle v^2_3\rangle/3$ in Eq. (26) and (b) for the consequence of second property in Eq. (28).

The resulting Eq. (27) is then reduced to

$${\rm KE}^{\rm 3D}_{\rm hs}/{\rm IE}^{\rm 3D}_{\rm hs} \simeq {\rm RKE}_{\rm tot}/(1 - {\rm RKE}_{\rm tot}). \quad (28)$$

However, the correlation of Eq. (28) is not strong as shown in Fig. (10)–(b) with an increasing number of outliers when $\ell = 1$ perturbations are intensified. Equation (25) becomes a unique function of the total residual kinetic energy,

$$\left(T^{\rm DT}_{\rm max}/T^{\rm DT}_{\rm min}\right)_{\ell=1} \simeq 1 + 4{\rm RKE}_{\rm tot}/(1 - {\rm RKE}_{\rm tot}), \quad (29)$$

which is inverted to give

$${\rm RKE}_{\rm tot} = \xi/(1 + \xi). \quad (30)$$

The ion-temperature measurement asymmetry parameter $\xi = (1/4)(R_T - 1) \geq 0$ is a function of the ion-temperature ratio $R_T = T^{\rm DT}_{\rm max}/T^{\rm DT}_{\rm min}$. Therefore, the yield degradation through Eq. (23) is an expression of the neutron-inferred ion-temperature measurement asymmetry parameter ξ,

$${\rm YOC} = [1 - \xi/(1 + \xi)]^{\mu}. \quad (31)$$

Equation (31) is simplified by fitting the YOC against the ion-temperature ratio in terms of a simple power law ${\rm YOC} = (R_T)^{-b_{\rm fit}}$. For the value of $\mu = 5$, the best fit is

$${\rm YOC} \approx \left(\frac{T^{\rm DT}_{\rm max}}{T^{\rm DT}_{\rm min}}\right)^{-1.53}. \quad (32)$$

For mid/high modes or fully turbulent flows, the anisotropic velocity variance decreases significantly, leading to small ion-temperature measurement variations among different LOS's. Simultaneously, the hot spot contains large isotropic flows, resulting in larger minimum neutron-inferred ion temperatures than the true thermal ion temperatures. The two fluid properties for mode $\ell = 1$ are not held by other modes in simulations because different flow structures have their own scalings for Eqs. (26) and (28).

To study Eqs. (31)–(32), *DEC3D* hydrodynamic data at stagnation, simulated by 1% to 14% initial velocity

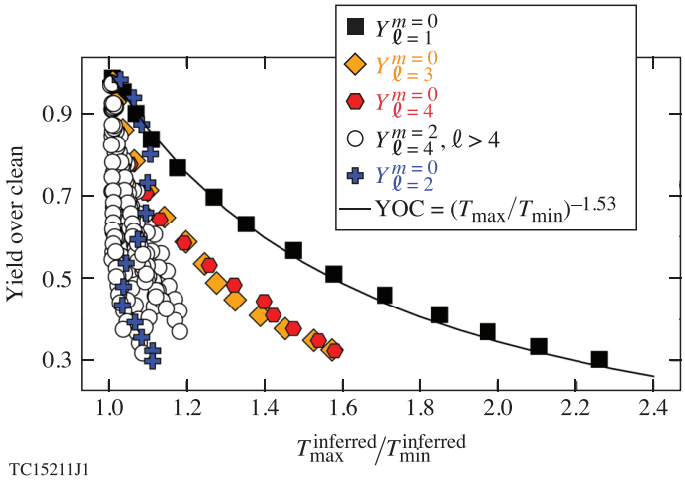

FIG. 11: Yield degradations versus ion-temperature measurement asymmetries for single modes. The black curve is given by Eq. (32).

perturbations, are post-processed by a Monte Carlo neutron transport code *IRIS3D*[11]. The ion temperatures are inferred from the width of neutron energy spectra using 16 detectors at LOS's distributed from the north to south poles uniformly at a fixed azimuthal angle $\phi = 0$ in *IRIS3D*. Figure (11) shows the yield degradation versus the neutron-inferred ion-temperature ratio. Result of mode $\ell = 1$ are shown accurately lying on the fitting curve given by Eq. (32). This is the first result to explain the yield degradation caused by mode 1 ion-temperature measurement asymmetries in terms of analytic models of residual kinetic energies and velocity variance analysis. In OMEGA implosion database, A. Lees showed that the fitting exponent was close to -1.3 by performing machine-learning data analysis. The close match of the fitting exponents implies the existence of mode $\ell = 1$ asymmetry in OMEGA database for implosions with ion temperature ratio $T_{max}/T_{min} > 1.1$. In general, the correlation between yield degradation and Ti asymmetry decreases with increasing isotropic flows. For instance, 2-D modes $\ell = 3$ to 4 exhibit a weaker Ti asymmetry because of decreasing anisotropic flows. Mode $\ell = 2$ and other mid/high modes $\ell > 4$ exhibit a much weaker Ti asymmetry because their high-velocity fluid motions driven by vorticity are located within cold bubbles, which contribute only negligible Doppler velocity broadening.

IV. CONCLUSION

In conclusion, a systematic analysis of 3-D effects of large isotropic flows on DD and DT neutron–inferred ion temperatures is presented. Strongly perturbed multimode perturbations are shown to produce a large content of isotropic flows within the hot spot, resulting in smaller DD than DT minimum neutron–inferred ion temperatures. The presence of large isotropic flows leads to the ratio of DD to DT minimum ion temperature approaching the lower bound of 0.8. The method to infer the DD minimum ion temperature through the removal of the anisotropic velocity variance is derived. The resulting DD minimum ion temperature is shown to demonstrate a strong correlation with the experimental fusion yields. A method to infer the DT thermal ion temperature through simultaneous DD and DT ion-temperature measurements at different LOS's is described. Reasonable agreement is observed with strongly perturbed multimode simulations. An analytic expression is derived to explain the anisotropic flow effect of ion-temperature measurement asymmetry on yield degradations for mode $\ell = 1$.

ACKNOWLEDGMENTS

This material is based upon work supported by the Department of Energy National Nuclear Security Administration under Award Number DE-NA0003856. This report was prepared as an account of work sponsored by an agency of the U.S. Government. Neither the U.S. Government nor any agency thereof, nor any of their employees, makes any warranty, express or implied, or assumes any legal liability or responsibility for the accuracy, completeness, or usefulness of any information, apparatus, product, or process disclosed, or represents that its use would not infringe privately owned rights. Reference herein to any specific commercial product, process, or service by trade name, trademark, manufacturer, or otherwise does not necessarily constitute or imply its endorsement, recommendation, or favoring by the U.S. Government or any agency thereof. The views and opinions of authors expressed herein do not necessarily state or reflect those of the U.S. Government or any agency thereof.

DATA AVAILABILTIY STATEMENT

The data that support the findings of this study are available from the corresponding author upon reasonable request.

Appendix A: Kinematics of neutrons

The relativistic motion of a single neutron along a straight line transport parallel to the LOS unit vector $\hat{d}$ is described as follows: Consider a Lorentz boost of a neutron momentum p_n in the CM frame of a DT ion pair by its CM frame velocity v_{cm}^{DT} relative to the neutron momentum p'_n observed in the fluid rest frame. Both p'_n and v_{cm}^{DT} are components parallel to $\hat{d}$:

$$p'_n = \gamma_{cm}(p_n + v_{cm}^{DT} E_n/c^2), \tag{A1}$$

where $E_{\rm n} = m_{\rm n}c^2 + K_{\rm n}$ is the total mass energy of the neutron in the CM frame, c is the speed of light, and $m_{\rm n}$ and $K_{\rm n}$ are the rest mass and the relativistic kinetic energy of the neutron in the CM frame, respectively. The Lorentz factor $\gamma_{\rm cm} = (1-\beta_{\rm cm}^2)^{-1/2}$ is a function of the DT ion-pair CM frame velocity through the factor of $\beta_{\rm cm} = v_{\rm cm}^{\rm DT}/c$. The kinetic energy of the neutron in the CM frame is obtained from the DT nuclear fusion energy release Q and the relative kinetic energy K of DT ions in their CM frame[21]:

$$\frac{p_{\rm n}^2}{2m_{\rm n}} = K_0 + \frac{\mu}{m_{\rm n}}K, \tag{A2}$$

where $K_0 = m_\alpha Q/(m_{\rm n}+m_\alpha) = m_{\rm n}v_0^2/2$ is the neutron birth energy and $\mu = m_{\rm n}m_\alpha/(m_{\rm n}+m_\alpha)$ is the reduced mass of DT fusion products. Let $p_0 = m_{\rm n}v_0$ be the neutron momentum at the zero DT relative kinetic energy limit $K=0$ and substitute $p_0 = \sqrt{2\mu Q}$ into Eq. (A2) to expand the neutron momentum $p_{\rm n} = p_0\sqrt{1+K/Q}$ with the relative kinetic energy K,

$$p_{\rm n} \simeq \left(1+\frac{K}{2Q}\right)p_0. \tag{A3}$$

Substitute Eq. (A3) into Eq. (A1) and expand the Lorentz factor $\gamma_{\rm cm} \simeq 1+\beta_{\rm cm}^2/2$ to first order to obtain the neutron momentum in the fluid rest frame,

$$p_{\rm n}' = p_0 + \frac{K}{2Q}p_0 + m_{\rm n}v_{\rm cm}^{\rm DT} + \triangle_1 + \triangle_2, \tag{A4}$$

where $\triangle_1 = \beta_{\rm cm}K_{\rm n}/c$ and $\triangle_2 = \beta_{\rm cm}^2(p_{\rm n} + v_{\rm cm}^{\rm DT}E_{\rm n}/c^2)/2$ are two relativistic correction terms. The neutron velocity $p_{\rm n}''$ observed in the laboratory frame parallel to $\hat{d}$ is obtained by the second Lorentz boost by the fluid velocity $\vec{v}$,

$$\vec{p}_{\rm n}'' \cdot \hat{v} = \gamma_v(\vec{p}_{\rm n}' \cdot \hat{v} + vE_{\rm n}'/c^2), \tag{A5}$$

$$\vec{p}_{\rm n}'' \cdot \hat{v}_\perp = \vec{p}_{\rm n}' \cdot \hat{v}_\perp, \tag{A6}$$

where $E_{\rm n}' = \gamma_v m_{\rm n}c^2$ is the total mass energy of the neutron in the fluid rest frame and $\gamma_v = (1-\beta_v^2)^{-1/2}$ is the Lorentz factor as a function of the fluid velocity through $\beta_v = v/c$. Here $\hat{v}_\perp$ is a unit vector perpendicular to the direction of the fluid velocity unit vector $\hat{v} = \vec{v}/v$. Only the component of the neutron momentum $\vec{p}_{\rm n}'' \cdot \hat{v}$ parallel to the fluid velocity is Lorentz boosted. Expand the Lorentz factor $\gamma_v \simeq 1+\beta_v^2/2$ and add Eqs. (A5) and (A6) together to obtain the neutron momentum vector $\vec{p}_{\rm n}'' = (\vec{p}_{\rm n}'' \cdot \hat{v})\hat{v} + (\vec{p}_{\rm n}'' \cdot \hat{v}_\perp)\hat{v}_\perp$ in the laboratory frame:

$$\vec{p}_{\rm n}'' = \vec{p}_{\rm n}' + m_{\rm n}\vec{v} + \frac{\beta_v^2}{2}\left[m_{\rm n}v + \vec{p}_{\rm n}' \cdot \hat{v} + vE_{\rm n}'/c^2\right]\hat{v}. \tag{A7}$$

Magnitudes of neutron momenta $p_{\rm n}'' = \vec{p}_{\rm n}'' \cdot \hat{d}$ and $p_{\rm n}' = \vec{p}_{\rm n}' \cdot \hat{d}$ parallel to $\hat{d}$ are obtained by taking a dot product on both sides of Eq. (A7):

$$p_{\rm n}'' = p_{\rm n}' + m_{\rm n}\vec{v} \cdot \hat{d} + \frac{\beta_v^2}{2}\left[m_{\rm n}v + \vec{p}_{\rm n}' \cdot \hat{v} + vE_{\rm n}'/c^2\right]\hat{v} \cdot \hat{d}. \tag{A8}$$

Non-relativistically with $\beta_v \to 0$ and $\triangle_1 = \triangle_2 \to 0$ in Eq. (A4), Eq. (A8) is reduced to a simple momentum addition $p_{\rm n}'' = p_{\rm n}' + m_{\rm n}\vec{v} \cdot \hat{d}$, where $p_{\rm n}'$ is given by Eq. (A4). The non-relativistic neutron velocity $v_{\rm n}'' = p_{\rm n}/m_{\rm n}''$ detected along $\hat{d}$

$$v_{\rm n}'' = v_0 + v_{\rm cm}^{\rm DT} + \kappa + \vec{v} \cdot \hat{d}. \tag{A9}$$

is the sum of the neutron birth velocity $v_0 = \sqrt{2K_0/m_{\rm n}}$, the DT center-of-mass velocity $v_{\rm cm}^{\rm DT}$ in the fluid rest frame that contributes to the primary thermal ion temperature, a small positive velocity shift $\kappa = v_0K/(2Q) > 0$ due to the DT relative kinetic energy, and a Doppler velocity shift $\vec{v} \cdot \hat{d}$ due to the fluid velocity in the nonstationary fusion plasma.

REFERENCES

[1] D. H. Munro, "Interpreting inertial fusion neutron spectra," Nucl. Fusion **56**, 036001 (2016).

[2] H. Brysk, "Fusion neutron energies and spectra," Plasma Phys. **15**, 611 (1973).

[3] T. J. Murphy, "The effect of turbulent kinetic energy on inferred ion temperature from neutron spectra," Phys. Plasmas **21**, 072701 (2014).

[4] M. Gatu Johnson, J. P. Knauer, C. J. Cerjan, M. J. Eckart, G. P. Grim, E. P. Hartouni, R. Hatarik, J. D. Kilkenny, D. H. Munro, D. B. Sayre, B. K. Spears, R. M. Bionta, E. J. Bond, J. A. Caggiano, D. Callahan, D. T. Casey, T. Döppner, J. A. Frenje, V. Y. Glebov, O. Hurricane, A. Kritcher, S. LePape, T. Ma, A. Mackinnon, N. Meezan, P. Patel, R. D. Petrasso, J. E. Ralph, P. T. Springer, and C. B. Yeamans, "Indications of flow near maximum compression in layered deuterium-tritium implosions at the national ignition facility," Phys. Rev. E **94**, 021202(R) (2016).

[5] B. K. Spears, M. J. Edwards, S. Hatchett, J. Kilkenny, J. Knauer, A. Kritcher, J. Lindl, D. Munro, P. Patel, H. F. Robey, and R. P. J. Town, "Mode 1 drive asymmetry in inertial confinement fusion implosions on the national ignition facility," Phys. Plasmas **21**, 042702 (2014).

[6] B. K. Spears, S. Glenzer, M. J. Edwards, S. Brandon, D. Clark, R. Town, C. Cerjan, R. Dylla-Spears, E. Mapoles, D. Munro, J. Salmonson, S. Sepke, S. Weber, S. Hatchett, S. Haan, P. Springer, E. Moses, J. Kline, G. Kyrala, and D. Wilson, "Performance metrics for inertial confinement fusion implosions: Aspects of the technical framework for measuring progress in the national ignition campaign," Phys. Plasmas **19**, 056316 (2012).

[7] L. Ballabio, J. KAllne, and G. Gorini, "Relativistic calculation of fusion product spectra for thermonuclear plasmas," Nucl. Fusion **38**, 1723 (1998).

[8] J. P. Chittenden, B. D. Appelbe, F. Manke, K. McGlinchey, and N. P. L. Niasse, "Signatures of asymmetry in neutron spectra and images predicted by three-dimensional radiation hydrodynamics simulations of indirect drive implosions," Phys. Plasmas **23**, 052708 (2016).

[9] K. M. Woo, R. Betti, D. Shvarts, O. M. Mannion, D. Patel, V. N. Goncharov, K. S. Anderson, P. B. Radha, J. P. Knauer, A. Bose,

V. Gopalaswamy, A. R. Christopherson, E. M. Campbell, J. Sanz, and H. Aluie, "Impact of three-dimensional hot-spot flow asymmetry on ion-temperature measurements in inertial confinement fusion experiments," Phys. Plasmas **25**, 102710 (2018).

[10]V. N. Goncharov, T. C. Sangster, R. Betti, T. R. Boehly, M. J. Bonino, T. J. B. Collins, R. S. Craxton, J. A. Delettrez, D. H. Edgell, R. Epstein, R. K. Follett, C. J. Forrest, D. H. Froula, V. Yu. Glebov, D. R. Harding, R. J. Henchen, S. X. Hu, I. V. Igumenshchev, R. Janezic, J. H. Kelly, T. J. Kessler, T. Z. Kosc, S. J. Loucks, J. A. Marozas, F. J. Marshall, A. V. Maximov, R. L. McCrory, P. W. McKenty, D. D. Meyerhofer, D. T. Michel, J. F. Myatt, R. Nora, P. B. Radha, S. P. Regan, W. Seka, W. T. Shmayda, R. W. Short, A. Shvydky, S. Skupsky, C. Stoeckl, B. Yaakobi, J. A. Frenje, M. Gatu-Johnson, R. D. Petrasso, and D. T. Casey, "Improving the hot-spot pressure and demonstrating ignition hydrodynamic equivalence in cryogenic deuterium–tritium implosions on omega," Phys. Plasmas **21**, 056315 (2014).

[11]F. Weilacher, P. B. Radha, and C. Forrest, "Three-dimensional modeling of the neutron spectrum to infer plasma conditions in cryogenic inertial confinement fusion implosions," Phys. Plasmas **25**, 042704 (2018).

[12]M. G. Johnson, J. A. Frenje, D. T. Casey, C. K. Li, F. H. Séguin, R. Petrasso, R. Ashabranner, R. M. Bionta, D. L. Bleuel, E. J. Bond, J. A. Caggiano, A. Carpenter, C. J. Cerjan, T. J. Clancy, T. Doeppner, M. J. Eckart, M. J. Edwards, S. Friedrich, S. H. Glenzer, S. W. Haan, E. P. Hartouni, R. Hatarik, S. P. Hatchett, O. S. Jones, G. Kyrala, S. Le Pape, R. A. Lerche, O. L. Landen, T. Ma, A. J. MacKinnon, M. A. McKernan, M. J. Moran, E. Moses, D. H. Munro, J. McNaney, H. S. Park, J. Ralph, B. Remington, J. R. Rygg, S. M. Sepke, V. Smalyuk, B. Spears, P. T. Springer, C. B. Yeamans, M. Farrell, D. Jasion, J. D. Kilkenny, A. Nikroo, R. Paguio, J. P. Knauer, V. Yu Glebov, T. C. Sangster, R. Betti, C. Stoeckl, J. Magoon, M. J. Shoup, G. P. Grim, J. Kline, G. L. Morgan, T. J. Murphy, R. J. Leeper, C. L. Ruiz, G. W. Cooper, and A. J. Nelson, "Neutron spectrometry—an essential tool for diagnosing implosions at the national ignition facility (invited)," Rev. Sci. Instrum. **83**, 10D308 (2012).

[13]D. H. Munro, J. E. Field, R. Hatarik, J. L. Peterson, E. P. Hartouni, B. K. Spears, and J. D. Kilkenny, "Impact of temperature-velocity distribution on fusion neutron peak shape," Phys. Plasmas **24**, 056301 (2017).

[14]O. Mannion, J. Knauer, V. Glebov, C. Forrest, A. Liu, Z. Mohamed, M. Romanofsky, T. Sangster, C. Stoeckl, and S. Regan, "A suite of neutron time-of-flight detectors to measure hot-spot motion in direct-drive inertial confinement fusion experiments on omega," Nuclear Instruments and Methods in Physics Research Section A: Accelerators, Spectrometers, Detectors and Associated Equipment , 163774 (2020).

[15]K. M. Woo, R. Betti, D. Shvarts, A. Bose, D. Patel, R. Yan, P.-Y. Chang, O. M. Mannion, R. Epstein, J. A. Delettrez, M. Charissis, K. S. Anderson, P. B. Radha, A. Shvydky, I. V. Igumenshchev, V. Gopalaswamy, A. R. Christopherson, J. Sanz, and H. Aluie, "Effects of residual kinetic energy on yield degradation and ion temperature asymmetries in inertial confinement fusion implosions," Phys. Plasmas **25**, 052704 (2018).

[16]J. Delettrez, R. Epstein, M. C. Richardson, P. A. Jaanimagi, and B. L. Henke, "Effect of laser illumination nonuniformity on the analysis of time-resolved x-ray measurements in uv spherical transport experiments," Phys. Rev. A **36**, 3926 (1987).

[17]A. L. Kritcher, D. E. Hinkel, D. A. Callahan, O. A. Hurricane, D. Clark, D. T. Casey, E. L. Dewald, T. R. Dittrich, T. Döppner, M. A. Barrios Garcia, S. Haan, L. F. Berzak Hopkins, O. Jones, O. Landen, T. Ma, N. Meezan, J. L. Milovich, A. E. Pak, H.-S. Park, P. K. Patel, J. Ralph, H. F. Robey, J. D. Salmonson, S. Sepke, B. Spears, P. T. Springer, C. A. Thomas, R. Town, P. M. Celliers, and M. J. Edwards, "Integrated modeling of cryogenic layered highfoot experiments at the nif," Physics of Plasmas **23**, 052709 (2016).

[18]K. Molvig, N. M. Hoffman, B. J. Albright, E. M. Nelson, and R. B. Webster, "Knudsen layer reduction of fusion reactivity," Phys. Rev. Lett. **109**, 095001 (2012).

[19]H.-S. Bosch and G. Hale, "Improved formulas for fusion cross-sections and thermal reactivities," Nuclear Fusion **32** (1992).

[20]A. L. Kritcher, R. Town, D. Bradley, D. Clark, B. Spears, O. Jones, S. Haan, P. T. Springer, J. Lindl, R. H. H. Scott, D. Callahan, M. J. Edwards, and O. L. Landen, "Metrics for long wavelength asymmetries in inertial confinement fusion implosions on the national ignition facility," Phys. Plasmas **21**, 042708 (2014).

[21]B. Appelbe and J. Chittenden, "The production spectrum in fusion plasmas," Plasma Phys. Control. Fusion **53**, 045002 (2011).